



## Article

\*Present address: Department of Physics and Technology, Faculty of Science and Technology, UiT The Arctic University of Norway, Tromsø, Norway.

**Cite this article:** Fisser H, Doulgeris AP, Høyland KV (2024). Impact of varying solar angles on Arctic iceberg area retrieval from Sentinel-2 near-infrared data. *Annals of Glaciology* 1–11. <https://doi.org/10.1017/aog.2024.39>

Received: 15 December 2023

Revised: 12 July 2024

Accepted: 7 October 2024

**Keywords:**

Icebergs; iceberg calving; remote sensing

**Corresponding author:**

Henrik Fisser;

Email: [henrik.fisser@uit.no](mailto:henrik.fisser@uit.no)

# Impact of varying solar angles on Arctic iceberg area retrieval from Sentinel-2 near-infrared data

Henrik Fisser<sup>1\*</sup> , Anthony P. Doulgeris<sup>1</sup>  and Knut V. Høyland<sup>2</sup>

<sup>1</sup>Department of Physics and Technology, Faculty of Science and Technology, UiT The Arctic University of Norway, Tromsø, Norway and <sup>2</sup>Department of Civil and Environmental Engineering, Faculty of Engineering, Norwegian University of Science and Technology, Trondheim, Norway

**Abstract**

Icebergs are part of the glacial mass balance and they interact with the ocean and with sea ice. Optical satellite remote sensing is often used to retrieve the above-waterline area of icebergs. However, varying solar angles introduce an error to the iceberg area retrieval that had not been quantified. Herein, we approximate the iceberg area error for top-of-atmosphere Sentinel-2 near-infrared data at a range of solar zenith angles. First, we calibrate an iceberg threshold at a 56° solar zenith angle with reference to higher resolution airborne imagery at Storfjorden, Svalbard. A reflectance threshold of 0.12 yields the lowest relative error of 0.19% ± 15.74% and the lowest interquartile spread. Second, we apply the 0.12 reflectance threshold to Sentinel-2 data at 14 solar zenith angles between 45° and 81° in the Kangerlussuaq Fjord, south-east Greenland. Here we quantify the error variation with the solar zenith angle for a consistent set of large icebergs. The error variation is then standardized to the error obtained in Svalbard. Up to a solar zenith angle of 65°, the mean standardized iceberg area error remains between 5.9% and −5.67%. Above 65°, iceberg areas are underestimated and inconsistent, caused by a segregation into shadows and sun-facing slopes.

**Introduction**

Icebergs are fragments of frozen freshwater calved from a glacier, ice sheet, or ice shelf. Iceberg calving is a variable in the glacial mass balance of marine-terminating glaciers that is associated with high uncertainties (Bigg and others, 1997; Enderlin and others, 2014; Amaral and others, 2020; Alley and others, 2023). By releasing freshwater icebergs may alter marine currents and nutrient concentrations (Azetsu-Scott and Syvitski, 1999; Dierking and Wesche, 2014; Moon and others, 2018; Sutherland and others, 2019; Rezvanbehbahani and others, 2020). Iceberg above-waterline areas are essential for iceberg drift and deterioration modeling (Keghouche and others, 2010; Marchenko and others, 2019; Monteban and others, 2020), to approximate marine freshwater fluxes (Sulak and others, 2017; Moon and others, 2018; Moyer and others, 2019; Rezvanbehbahani and others, 2020; Schild and others, 2021; Shiggins and others, 2023), and nutrient fluxes (Bhatia and others, 2013; Duprat and others, 2016). Maritime engineering and operational ice charting need iceberg size distributions for safe Arctic operations (Bobby and Power, 2023). The area-frequency distribution of iceberg populations can be typically described by a power-law distribution near the calving front, and by a log-normal distribution in open water (Kirkham, 2017).

Satellite remote sensing is invaluable for retrieving iceberg areas (Sulak and others, 2017; Moyer and others, 2019; Neuhaus and others, 2019; Scheick and others, 2019). Though, errors in the observed iceberg areas can lead to skewed size distributions (Scheick and others, 2019) and propagate into estimates upon the iceberg areas.

Satellite synthetic aperture radar (SAR) data are often used to detect icebergs (Power and others, 2001; Dierking and Wesche, 2014; Marino and others, 2016; Tao and others, 2016; Soldal and others, 2019; Færch and others, 2023) due to their independence from weather and solar illumination. Buus-Hinkler and others (2014) showed for Sentinel-1 SAR data with reference to optical Landsat data that iceberg areas retrieved from the SAR data are inaccurate. The error in the iceberg area retrieval from SAR can be partly, however not fully, explained by the limit in the spatial resolution (Buus-Hinkler and others, 2014). The high resolution of currently available non-commercial optical satellite data, low noise levels, the absence of SAR speckle, and the less variable and less ambiguous signals of ocean and ice surfaces are advantages of these data. Here we argue for leveraging the growing archive of high resolution SAR data for the iceberg area retrieval supported by higher resolution optical data. However, this requires understanding errors in the iceberg area retrieval from optical satellite data.

Low sun angles at high latitudes challenge the iceberg area retrieval from optical satellite data. The European Space Agency (2019) recommends using Sentinel-2 data acquired below a solar zenith angle (Fig. 1) of 70°. While some studies limited the iceberg area retrieval accordingly, we recognize the need to maximize the temporal bounds. Moyer and others (2019) used Sentinel-2 data acquired above a solar zenith angle of 70°, adjusting the threshold to the different illumination conditions. On sea ice, Kern (2022) recognized inconsistencies

© The Author(s), 2024. Published by Cambridge University Press on behalf of International Glaciological Society. This is an Open Access article, distributed under the terms of the Creative Commons Attribution licence (<http://creativecommons.org/licenses/by/4.0/>), which permits unrestricted re-use, distribution and reproduction, provided the original article is properly cited.

[cambridge.org/aog](https://cambridge.org/aog)



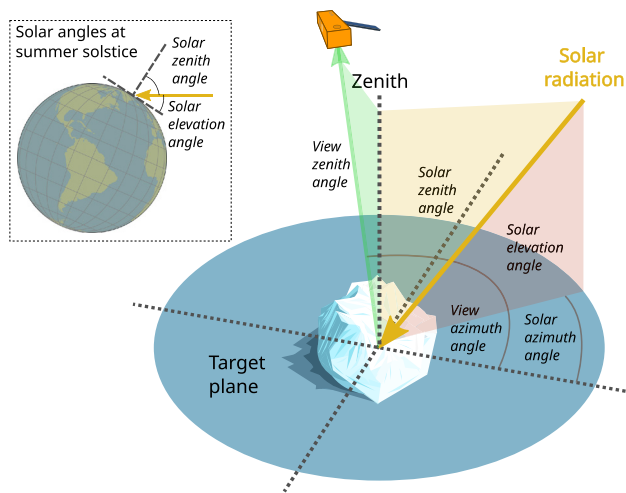


**Figure 1.** Solar angles and viewing geometry of a passive satellite sensor with respect to an iceberg on a target plane. The paper focuses on the variation in the solar zenith angle, which is a function of the time of the day, the time of the year, and the latitude.

due to varying illumination conditions in Landsat data already below a solar zenith angle of  $65^\circ$ . The literature appears unclear regarding a sensible illumination limit for the iceberg area retrieval from optical satellite data. In this paper we therefore address the impact of the varying solar illumination on the iceberg area retrieval from Sentinel-2 near-infrared data.

### Optical remote sensing of Arctic icebergs

Many have detected and delineated icebergs in optical satellite data across spatial and temporal scales (Williams and Macdonald, 1995; Kirkham, 2017; Sulak and others, 2017; Moyer and others, 2019; Neuhaus and others, 2019; Scheick and others, 2019; Monteban and others, 2020; Rezvanbehbahani and others, 2020). An early attempt used a segmentation approach in the first years of the Landsat mission (Williams and Macdonald, 1995). It is most common to apply an absolute reflectance threshold to one or several spectral bands to detect icebergs observed in optical remote sensing data (Sulak and others, 2017; Moyer and others, 2019; Neuhaus and others, 2019; Scheick and others, 2019; Rezvanbehbahani and others, 2020). This approach is usually able to distinguish icebergs from open water, but icebergs may be confused with sea ice (Sulak and others, 2017). A related approach exploits the contrast between the surrounding ocean and the iceberg (Kirkham, 2017). Rezvanbehbahani and others (2020) showed that a convolutional neural network is less prone to false detections of highly reflective non-iceberg surfaces in ice mélange.

Iceberg areas are sensitive to the reflectance threshold used to detect and delineate icebergs in optical data. Scheick and others (2019) found a sensible balance between true and false positive icebergs at a 0.19 reflectance threshold applied to panchromatic Landsat top-of-atmosphere (TOA) data acquired between May and October. With reference to Sulak and others (2017), Scheick and others (2019) found overestimated total iceberg areas at varying magnitudes in different Greenlandic fjords. Moyer and others (2019) proposed a 0.13 reflectance threshold applied to TOA Sentinel-2 near-infrared (NIR) data. At a solar zenith angle of  $47^\circ$  the study implies an average overestimation of iceberg areas by 4% with reference to higher resolution optical satellite imagery. Rezvanbehbahani and others (2020) adopted the 0.13 reflectance threshold to estimate marine fresh-water fluxes.

### Solar angle effects on optical measurements of glacier ice, snow, water

Studying optical measurements of icebergs floating in open water primarily encounters three materials: Glacier ice, snow, and liquid water. Open water exhibits specular reflections and hence reflects about 0.5% of the downwelling shortwave radiation to a sensor (Pegau and Paulson, 2001). The reflectance of open water rises steeply above solar zenith angles of about  $70^\circ$ , with an increasing variation caused by wind speed (Pegau and Paulson, 2001). Glacier ice and snow reflect strongly at visual and near-infrared wavelengths, and their reflectance decreases above  $\sim 600$  nm (Warren, 2019). At wavelengths between 500 nm and 1500 nm, the size and concentration of air bubbles and cracks drive the reflectance of glacier ice. Scattering occurs at the interface of the ice and the air bubbles. Thus, a higher concentration or size of these bubbles increases the reflectance (Gardner and Sharp, 2010). The snow reflectance varies with the snow thickness, density, age, the air temperature, and the grain size. Contaminants such as dust or ash dampen the glacier ice and snow reflectance (Gardner and Sharp, 2010; Warren, 2019).

The incidence angle of the solar illumination impacts the reflectance of glacier ice, snow, and water. The solar elevation  $\phi$  is the angle between a point on the earth surface and the sun (Fig. 1). The solar zenith angle  $\theta$  is the angle between the zenith at a given point and the sun:

$$\theta = 90 - \phi. \quad (1)$$

The lowest solar zenith angle is reached at the summer solstice.

The open water broadband albedo under clear sky increases following a mathematical logistic curve as  $\theta$  rises. Additionally, at high solar zenith angles, the albedo is negatively related to wind speed (Pegau and Paulson, 2001; Huang and others, 2019). We expect the surface albedo of snow and ice to increase non-linearly towards higher solar zenith angles (Robock, 1980; Gardner and Sharp, 2010; Whicker and others, 2022), although, surface roughness can decrease the albedo at high solar zenith angles due to shadowing (Gardner and Sharp, 2010; Kern, 2022).

### Solar angle effects on iceberg area retrievals

When retrieving iceberg areas via a reflectance threshold applied to optical data, the threshold choice affects the number of detected small icebergs and the obtained iceberg sizes (Sulak and others, 2017; Moyer and others, 2019; Scheick and others, 2019; Rezvanbehbahani and others, 2020). Additionally, high solar zenith angles challenge the threshold choice due to increasingly variable reflectance measurements of open water and ice (Moyer and others, 2019; Kern, 2022). In addition to the solar zenith angle, the viewing geometry of a passive sensor relative to the target plane influences the measurement (Fig. 1).

To address varying solar angles, Moyer and others (2019) raised their 0.13 threshold derived at  $\theta \sim 47^\circ$  to 0.3 in autumn. Rezvanbehbahani and others (2020) limited their study to low solar zenith angles in high summer. Other studies derived iceberg areas over several months without specifically accounting for varying solar zenith angles (Sulak and others, 2017; Scheick and others, 2019). It appears unclear how variations in the solar zenith angle affect the accuracy of iceberg areas obtained from optical satellite remote sensing data. Moyer and others (2019) accounted to some extent for the illumination variation. However, it is uncertain how adapting the threshold affects the iceberg area error. Quantifying this error is important to understand temporal limits for the iceberg area retrieval from optical satellite data, imposed by the solar angles. In this paper we hence approximate

the error in iceberg areas retrieved from optical Sentinel-2 NIR data between solar zenith angles of  $45^\circ$  and  $81^\circ$ .

### Study outline

We report on two connected experiments centered around Sentinel-2 data in Svalbard and south-east Greenland. The experiments address iceberg areas retrieved from Sentinel-2 data spanning summer and autumn months, in open water settings.

In the first experiment, we calibrated the Sentinel-2 iceberg NIR reflectance threshold and quantified the iceberg area error at a single solar zenith angle. The calibration was done with reference to iceberg areas derived from optical data acquired during an airborne campaign in Storfjorden, Svalbard, sampled at a 6.25 times finer resolution than the Sentinel-2 satellite data. In the second experiment, we quantified the variation of the iceberg area error with the solar zenith angle. For this purpose, the NIR threshold was applied at 14 solar zenith angles in the Kangerlussuaq Fjord, south-east Greenland. We quantified an iceberg area error at every solar zenith angle with reference to visually delineated large icebergs. The Svalbard experiment calculates an error magnitude over a range of iceberg sizes, whereas the Greenland experiment provides the error variation with the solar zenith angle. Therefore, we standardized the area error from the Greenland experiment to the error obtained in Svalbard experiment. This step approximated the Sentinel-2 iceberg area error for solar zenith angles ranging from  $45^\circ$  to  $81^\circ$ .

### Data

#### Sentinel-2 data

The Copernicus Sentinel-2 mission consists of two satellites launched in 2015 and 2017. Their Sentinel-2 Multispectral Instrument measures the reflected solar spectral radiances between 443 and 2222 nm central band wavelengths in a 290 km swath (ESA, 2023).

Sentinel-2 level 1C acquisitions with a scene cloud cover below 2% were searched. Acquisitions were dropped when the visually estimated sea ice concentration exceeded roughly 10%. The solar zenith angle  $\theta$  was calculated in the center of each acquisition using the pysolar software (Stafford, 2023). The processing of

the Sentinel-2 to the processing level 1C by ESA has changed over time, resulting in different processing baselines. The data are distributed in digital numbers (DNs) that have to be converted to reflectance data. Products with a processing baseline above 4.0 require subtracting a constant radiometric offset of 1000 from the DN (ESA, 2024), which was done prior to the conversion to TOA reflectances. The data were then converted to TOA reflectances  $\rho_{TOA}$  by applying the coefficient of  $10^{-4}$  to the DN values. The Sentinel-2 data analyzed in this study are TOA reflectance values ranging from 0 to the saturation value of 1. We did not employ a marine atmospheric correction method to avoid potentially added ambiguities (König and others, 2019). A cloud probability map was calculated using the *s2cloudless* algorithm (Skakun and others, 2022), and probabilities above 5% were flagged as clouds. The NIR band (B8), denoted  $\rho_{NIR}$ , is measured at a 833 nm wavelength with a 105 nm bandwidth, and sampled at a 10 m spatial resolution (ESA, 2023). We used only  $\rho_{NIR}$  as it contains less atmospheric scattering than the other 10 m resolution bands.

#### Storfjorden, Svalbard

The variation in the iceberg area error with iceberg size was quantified at Storfjorden, East Svalbard (Fig. 2). Negribreen and Sonklarbreen are two tidewater glaciers calving into Storfjorden. The Sentinel-2 tile identifiers covering the Dornier flight paths are 33XWH and 33XXH, acquired approximately at 14:17 pm local time (12:17 UTC) on 21 June 2021 at  $\theta \sim 56^\circ$ .

#### Kangerlussuaq Fjord, south-east Greenland

The variation in the iceberg area error with the solar zenith angle was quantified in the Kangerlussuaq Fjord in south-east Greenland in the Sentinel-2 tile 25WER (Fig. 2). The Kangerlussuaq glacier accounts for 5% of the mass balance of the Greenland ice sheet (Enderlin and others, 2014). We chose this fjord due to a consistent and large iceberg population in open water during summer months. 14 acquisitions were gathered at solar zenith angles between  $45^\circ$  and  $81^\circ$  (Table 1).

#### Optical airborne data, Svalbard

Optical airborne imagery in the visual bands was collected by a PhaseOne IXU-150 camera mounted on a Dornier aircraft. The

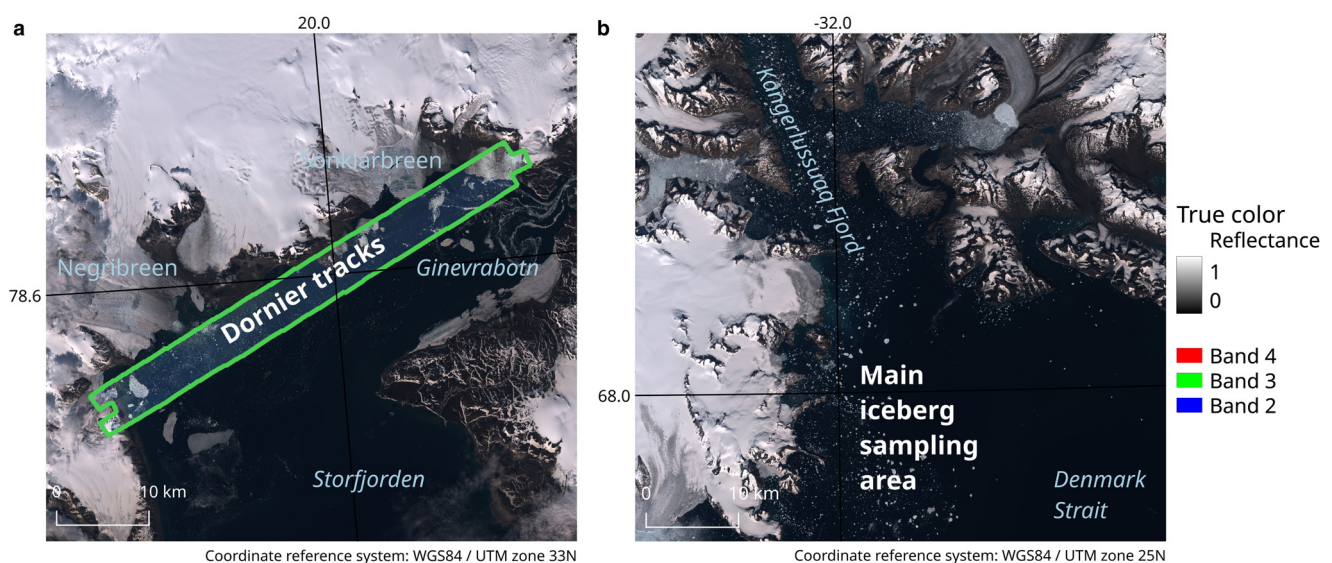


**Figure 2.** Maps of the study sites, Storfjorden (a) and Kangerlussuaq Fjord (b). The Storfjorden map shows the Sentinel-2 acquisition on 21 June 2020 at  $78.69710^\circ\text{N}$ ,  $19.80409^\circ\text{E}$ , overlaid by the Dornier tracks. The Sentinel-2 acquisition in the Kangerlussuaq map was acquired on 27 July 2018 at  $67.94712130^\circ\text{N}$ ,  $-31.60573189^\circ\text{W}$ .



**Table 1.** Sentinel-2 data, Kangerlussuaq fjord, sorted by  $\theta$ 

	$\theta$ (°)	Year	Month	Day	Time (UTC)
1	45	2020	7	4	14:25
2	47	2016	7	20	14:10
3	49	2018	7	27	16:09
4	52	2017	8	9	14:13
5	56	2020	8	20	16:10
6	58	2020	8	25	17:47
7	60	2017	8	31	14:00
8	62	2017	9	7	13:50
9	64	2017	9	13	14:10
10	67	2018	9	20	17:52
11	70	2019	9	28	14:24
12	73	2021	10	6	14:13
13	75	2020	10	9	14:29
14	81	2020	10	26	14:12

acquisition was done in the northern part of Storfjorden, Svalbard, on 21 June 2020 starting at 3:20 pm local time (1:20 UTC), about an hour after the Sentinel-2 acquisitions. The data were georeferenced and downsampled to 4 m spatial resolution post flight.

### Meteorological reanalysis data

We gathered 2 m air temperature simulations from the Arctic Regional Reanalysis (CARRA) product (Schyberg, 2020). The data were downloaded from the Copernicus Climate Change Service C3S Climate Data Store (2021). The current version of the CARRA dataset relies on the HARMONIE-AROME cycle 40h1.1, and is vertically forced by the ERA5 dataset (Költzow and others, 2022). The spatial resolution of the CARRA dataset is 2.5 km, and simulations are available every three hours. The closest simulations to the Sentinel-2 timestamps were selected.

### Methods

In this study we used two connected experiments to quantify the iceberg area error from Sentinel-2 NIR data as a function of the solar zenith angle. The Svalbard experiment determined a NIR reflectance threshold for delineating iceberg areas, and quantified the iceberg area error for icebergs with lengths between 14 and 149 m. The Greenland experiment quantified the variation in

the iceberg area error with the solar zenith angle. By standardizing the error variation (Greenland) to the error magnitude and spread (Svalbard), we yielded the standardized iceberg area error between solar zenith angles of 45° and 81°. The subsequent section explains the steps leading to the standardized iceberg area error as summarized in Fig. 3.

### Sentinel-2 iceberg detection

We detected icebergs by testing every pixel in the  $\rho_{NIR}$  data against a reflectance threshold (Sulak and others, 2017; Scheick and others, 2019; Moyer and others, 2019; Rezvanbehbahani and others, 2020). The threshold was varied in the Svalbard experiment; details are described subsequently. The measurements above the threshold were flagged as iceberg pixels. Adjacent pixels are considered to belong to the same iceberg. An iceberg detection is a polygon geometry delineating the connected pixels.

### Iceberg area error metrics

Iceberg areas were calculated in  $m^2$ . However, the square root of the areas (m) is reported in this study when applicable to provide an approximate length scale, referred to as *root length*. All error metrics were calculated upon the area values. The Dornier iceberg areas are denoted as  $A_{DO}$  and the Sentinel-2 iceberg areas as  $A_{S2}$ . The relative error  $RE$  between reference iceberg areas and the Sentinel-2 iceberg areas was calculated in both experiments. In the Svalbard experiment, the reference is the set of Dornier iceberg areas. In Greenland, the reference is the set of visually delineated icebergs. We derived the relative error  $RE$  in percentage:

$$RE = 100 \cdot \frac{A_{S2} - A_{reference}}{A_{reference}}. \quad (2)$$

A positive  $RE$  implies an overestimation by Sentinel-2 compared to the reference area.

### Iceberg threshold calibration

The Svalbard experiment aimed to quantify an iceberg area error over a range of iceberg sizes (Fig. 3). As part of this experiment a suitable NIR-threshold was chosen based on a sensitivity analysis. The reference icebergs were delineated in higher resolution

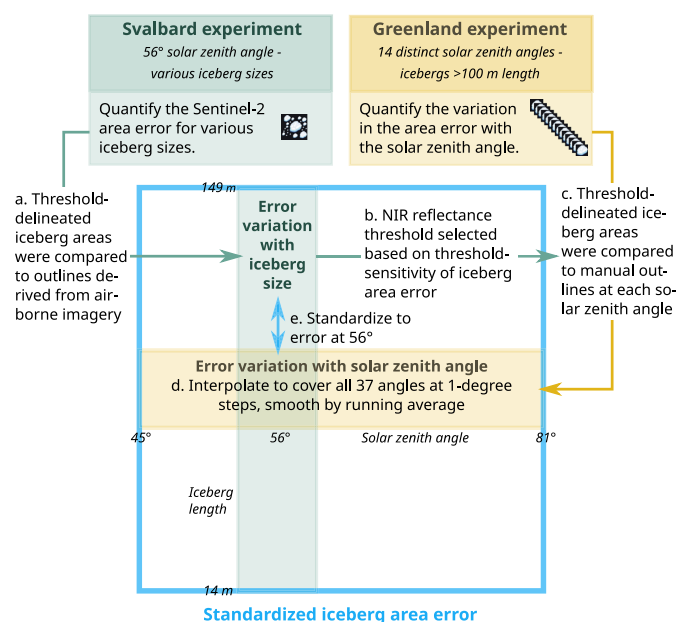


**Figure 3.** The two connected experiments aimed to derive a standardized iceberg area error for Sentinel-2 data, applicable over a range of iceberg sizes and solar zenith angles. The blue box depicts the limits of the error with respect to the iceberg sizes covered by the Svalbard experiment, and the solar zenith angles covered by the Greenland experiment.

airborne imagery at a single solar zenith angle. The iceberg area error was calculated by directly comparing the airborne iceberg areas with the iceberg areas derived from the Sentinel-2 data (Fig. 3a). The high resolution of the airborne imagery allows a visual delineation of icebergs in the imagery. To speed up the delineation we applied a rough initial threshold that separates icebergs from open water in the 8-bit imagery with digital numbers between 0 and 255. A threshold of 127.5 (50% of the maximum digital number) was applied to the three bands red, green, and blue to obtain an initial delineation of icebergs in the fjord. This threshold was approximately the center between the low ocean measurements ( $DN \leq 100$ ) and the high ice measurements ( $DN \geq 150$ ). The rough threshold only yielded an initial delineation of ice in the fjord. We then refined the delineations visually when darker parts of the icebergs had not been captured by the initial threshold. To examine the sensitivity of the area error to the NIR threshold, (Fig. 3b), icebergs were detected and delineated in the Sentinel-2 data at a range of reflectance thresholds between 0.06 and 0.22. These thresholds were applied to the  $\rho_{NIR}$  reflectance data that were scaled between 0-1. For this direct comparison we had to account for the drift between the data acquisitions. Usually we observed drift distances on a 100 m scale. While the start of the Dornier acquisition was one hour after the Sentinel-2 acquisition, the exact time lag increases along the flight tracks. The matching was done visually, using the Sentinel-2 icebergs that were detected at the lowest threshold. Finally, the iceberg areas of the Sentinel-2 icebergs were compared to the Dornier iceberg areas at each NIR threshold. The threshold with the lowest iceberg area error was chosen and applied in the Greenland experiment (Fig. 3b).

### Iceberg area error by solar zenith angle

The Greenland experiment aimed to quantify an iceberg area error over a range of solar zenith angles (Fig. 3). The objective was to quantify the error in the iceberg area retrieval over multiple iceberg sizes in the Svalbard experiment, whereas the Greenland experiment quantifies the error variation with  $\theta$ . The underlying issue was that the airborne data did not cover a range of solar zenith angles. Furthermore, visually deriving reliable iceberg outlines directly from the Sentinel-2 data is only possible for large icebergs relative to the Sentinel-2 resolution. Therefore, the Greenland experiment featured large icebergs only, creating a consistent dataset that is comparable over time.

### Reference iceberg areas

We visually delineated a total of 378 large and very large icebergs, 27 in each Sentinel-2 acquisition, spanning 14 solar zenith angles in the Kangerlussuaq Fjord. The visually delineated areas were compared to the areas delineated by the NIR reflectance threshold (Fig. 3c). To obtain a consistent dataset, we only delineated icebergs with a *root length* above 100 m. This strategy was employed for two reasons. First, icebergs of this size can be visually delineated in the Sentinel-2 data because spectrally mixed measurements at the edge constitute a smaller proportion of the entire iceberg area. Second, it was only possible to clearly identify shadows at this large size relative to the 10 m resolution of the Sentinel-2 data. On smaller icebergs the spectral mixing at the edge blurs shadows, impeding a reliable delineation that can be trusted as a reference. The visually derived outlines are assumed to cover the entire icebergs above the waterline. In addition, to examine the reflectance measurements of the iceberg and the surrounding water, a 100 m wide buffered belt was created around each outline, covering the iceberg neighborhood. All  $\rho_{NIR}$  measurements were gathered separately within the iceberg outline, and in the neighborhood for statistical analysis.

### Standardizing the area error to the Svalbard calibration

The Svalbard experiment quantified the magnitude of the relative area error across iceberg sizes. The Greenland experiment quantified the error variation with the solar zenith angle, but limited to large icebergs. The relative error  $RE_{\theta}$  was calculated for the iceberg pairs at every solar zenith angle. Constrained by the available cloud-free data (Table 1), the solar zenith angles in our dataset are regularly but not equally spaced. Hence we interpolated the  $RE_{\theta}$  linearly in  $1^{\circ}$  steps between  $45^{\circ}$  and  $81^{\circ}$ :

$$f(\theta_i) = RE_{\theta_a} + (\theta_i - \theta_a) \cdot \left( \frac{RE_{\theta_b} - RE_{\theta_a}}{\theta_b - \theta_a} \right) \quad (3)$$

with  $a$  and  $b$  being the indices of the closest lower and higher  $\theta$  value pair, respectively. The interpolation function  $f(\theta_i)$  was applied at every  $\theta$ , yielding an  $RE_{\theta}$  value in degree-steps between  $45^{\circ}$  and  $81^{\circ}$ . It can be reasonably assumed that the changes in  $RE_{\theta}$  with a rising solar zenith angle are gradual. However, despite our endeavor to obtain a consistent and comparable iceberg dataset across solar zenith angles, unreasonable oscillations still appeared in  $RE_{\theta}$ . To smooth these oscillations, we derived running averages in a window of five degrees centered at a specific  $\theta_x$ :

$$\widetilde{RE}_{\theta_x} = \frac{1}{5} \cdot \sum_{i=x-2}^{k=x+2} f(\theta_i), \quad (4)$$

producing the smooth error  $\widetilde{RE}_{\theta}$  in  $1^{\circ}$  steps (Fig. 3d). The averaging at the lower ( $45^{\circ}$ ,  $46^{\circ}$ ) and upper limits ( $81^{\circ}$ ,  $80^{\circ}$ ) lacks lower or upper samples, respectively. Here the running average is based on the three or four available values.

We understand the Svalbard  $RE$  as the error magnitude at  $56^{\circ}$ , whereas the Greenland experiment depicts its variation with the solar zenith angle. Hence, the smooth error was standardized to the mean error  $\overline{RE}$  that was derived in the Svalbard calibration at  $56^{\circ}$ . We scaled  $\widetilde{RE}_{\theta}$  linearly with reference to  $\widetilde{RE}_{\theta_{56}}$  at  $56^{\circ}$ :

$$SRE_{\theta} = \widetilde{RE}_{\theta} - \widetilde{RE}_{\theta_{56}} + \overline{RE}, \quad (5)$$

resulting in the standardized iceberg area error  $SRE_{\theta}$  (Fig. 3e). The 25<sup>th</sup> and 75<sup>th</sup> percentiles were equivalently standardized to the percentiles at the  $56^{\circ}$  solar zenith angle. At  $\theta = 56^{\circ}$ , the standardized iceberg area error thus has the mean value and the interquartile range obtained at that  $\theta$  in the Svalbard experiment. The variation with  $\theta$  stems from the Greenland experiment.

## Results

We first examine the iceberg threshold calibration in the Svalbard experiment. Next, we analyze the variation of the Sentinel-2 iceberg reflectance measurements with the solar zenith angle observed in the Greenland experiment. Finally, we present the standardized iceberg area error for solar zenith angles between  $45^{\circ}$  and  $81^{\circ}$ .

### Iceberg threshold calibration

The lowest relative error magnitude was yielded at a 0.12  $\rho_{NIR}$  detection threshold, suggesting this as the most suitable threshold for the iceberg area retrieval from these data. At this threshold the mean  $RE$  is  $0.19\% \pm 15.74\%$ . The MAE is  $303.33 \text{ m}^2 \pm 306.27 \text{ m}^2$ , corresponding to about three Sentinel-2 pixels at a 10 m resolution.

The highest positive and negative  $RE$  values are observed at the low and high end of the tested threshold range (Fig. 4). Correspondingly, the interquartile range tends to increase below

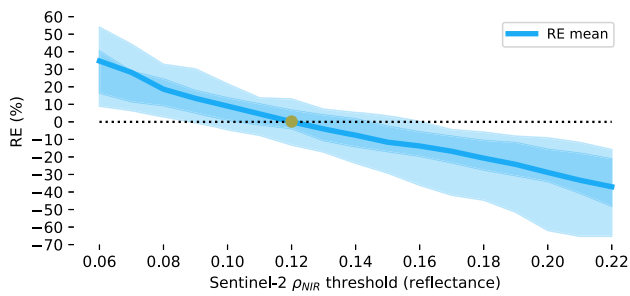


**Figure 4.** The *RE* by the Sentinel-2  $\rho_{NIR}$  threshold. The green dot marks the lowest error magnitude. The dark shaded area covers the interquartile range. The light shaded area covers the range between the 10<sup>th</sup> (P10) and the 90<sup>th</sup> (P90) percentiles.

**Table 2.** Iceberg root length (m) statistics Dornier & Sentinel-2

	Mean	Q1	Q2	Q3	Min	Max
DO	63.04	41.27	51.35	76.13	29.74	148.99
S2	62.82	42.43	51.82	78.2	20.0	145.26
Difference	0.22	-1.16	-0.47	-2.07	9.74	3.73

and above the 0.12 threshold, which exhibits the lowest spread among all thresholds (Fig. 4).

#### Area error at the 0.12 reflectance threshold

Here we report results obtained at the 0.12 reflectance threshold. The mean iceberg areas of the matched icebergs are close, but larger differences are seen at the margins of the distribution (Table 2).

The iceberg area distributions are consequently similar, both following a typical distribution with a higher abundance of small icebergs as compared to large icebergs (Fig. 5).

The Sentinel-2 and Dornier iceberg areas exhibit a very strong linear correlation with Pearson's *r*-value close to 1 and consistent slope and intercept (Fig. 6). Despite the linear agreement, individual icebergs in Fig. 6 deviate in positive and negative directions. To examine *RE* variations with the reference iceberg size, the Dornier iceberg samples were grouped into area bins (Fig. 7).

The standard deviation of the *RE* in the smallest area bin is roughly 19 times the standard deviation in the largest area bin, and the P10-P90 spread is greater, accordingly. This suggests that the *RE* is more consistent for larger icebergs while the area of smaller icebergs tends to be more erroneous.

#### Iceberg area error by solar zenith angle

The mean root length of all reference iceberg areas in the Greenland experiment is  $326.94 \text{ m} \pm 26.15 \text{ m}$ , ranging from 103.27 m to 712.79 m. These statistics summarize all 378 icebergs

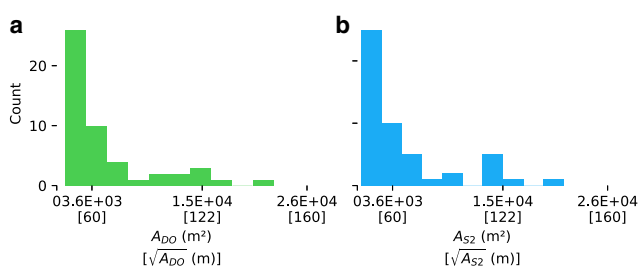


**Figure 5.** Area distributions for icebergs sampled in the Dornier data (a), and for the identical icebergs delineated by the reflectance threshold applied to Sentinel-2 NIR data (b).

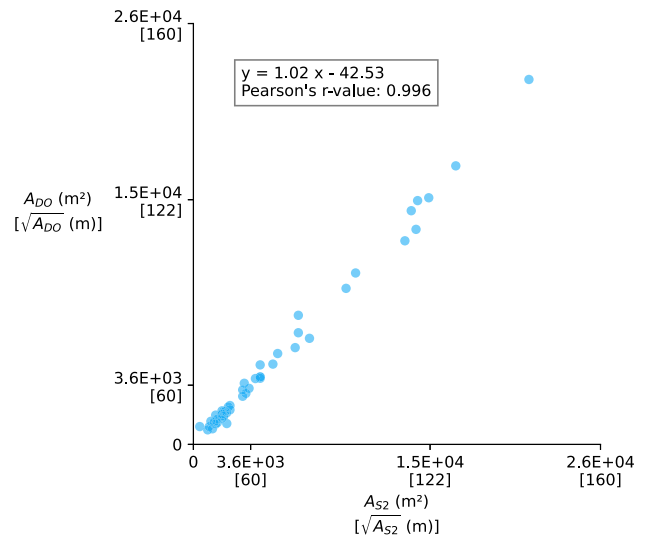


**Figure 6.** The Sentinel-2 and Dornier iceberg areas at the 0.12 threshold. The root length is provided below the labels on the x-axis.

present in the Greenland dataset. Keep in mind that only large icebergs were sampled in Greenland to create a consistent and comparable dataset over 14 solar zenith angles. The Greenland experiment aimed to quantify the variation in the iceberg area error with the solar zenith angle. Subsequently, the emphasis is therefore on the relative changes in the iceberg reflectance, and changes in the area error with the solar zenith angle. Finally, the standardized iceberg area error is presented, which contains the error magnitude quantified in the Svalbard experiment, and its variation quantified in the Greenland experiment.

#### Reflectance measurements

At each solar zenith angle, we obtained two sets of  $\rho_{NIR}$  measurements: the icebergs and their neighborhoods. Furthermore, the mean 2 m air temperature was taken from the CARRA dataset as the air temperature may affect the reflectance of snow and ice. The mean 2 m air temperature was  $2.04^\circ\text{C}$  with two dates below freezing (Fig. 8).

Up to a solar zenith angle of  $58^\circ$ , the mean reflectance centers around the mean over all 37 values. Above  $58^\circ$ , it varies below the mean, and reaches a minimum at  $70^\circ$  (Fig. 8). This minimum coincides with a positive spike in the air temperature. Past  $70^\circ$ , the mean iceberg reflectance rises, leveling out at  $75^\circ$  (Fig. 8). The single mode seen in the reflectance histograms (Fig. 9) flattens above  $64^\circ$ . Correspondingly, the standard deviation rises and the distribution becomes right-skewed (Fig. 10). A cluster of saturated samples develops at the high reflectance end from

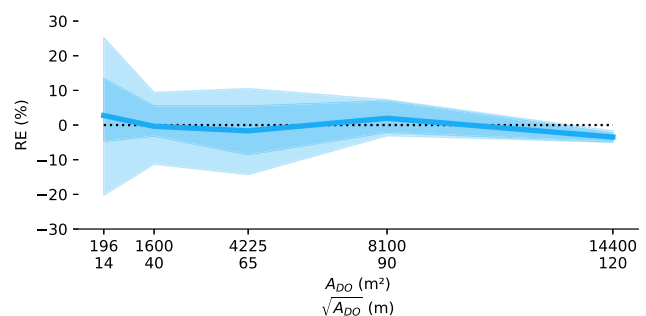


**Figure 7.** The *RE* in Dornier area bins. The dark shaded area covers the interquartile range. The light shaded area covers the P10-P90 range. The root length is provided below the labels on the x-axis.

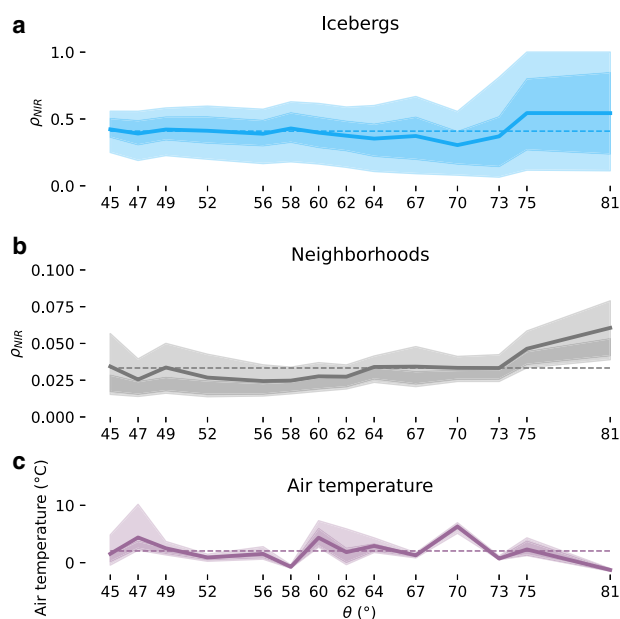


**Figure 8.** Iceberg (a) and neighborhood (b)  $\rho_{NIR}$  by the solar zenith angle, and the air temperature (c). The dashed lines indicate the mean over all 37 values. The dark shaded areas cover the interquartile ranges. The light shaded areas cover the P10-P90 ranges. Note the distinct scaling on the y-axes of the two top subplots.

67°. The iceberg reflectance becomes multimodal above 70° with a skewness approaching zero (Fig. 10).

#### Area error

The Greenland experiment calculated the  $RE_{\theta}$  (Fig. 11), which was standardized to the  $RE$  quantified in the Svalbard experiment. The result is the standardized iceberg area error  $SRE_{\theta}$  (Fig. 11) describing the magnitude and the variation in the iceberg area error when delineating icebergs by the NIR threshold proposed in this study.

We identify three  $SRE_{\theta}$  regimes. In the first error regime up to 65°, the mean  $SRE_{\theta}$  ranges between 5.9% and -5.67%. The first

error regime is split into positive mean  $SRE_{\theta}$  values up to 56°, and negative values up to 65°. The interquartile spread increases with the solar zenith angle.

In the second error regime from 66° to 72°, the mean  $SRE_{\theta}$  drops to reach its largest negative value at 72°, while the interquartile error spread increases steadily. In the third error regime from 73°, the mean  $SRE_{\theta}$  rises towards 0. The interquartile spread flattens, and the upper  $SRE_{\theta}$  quartile becomes positive from 76° (Fig. 11).

#### Discussion

In this paper we approximated the error in the iceberg area retrieval from Sentinel-2 data as a function of iceberg size and the solar zenith angle. We first calibrated the iceberg NIR reflectance threshold based on airborne imagery in Svalbard, and quantified the iceberg area error for iceberg sizes with root lengths ranging from 14 to 149 m. We then quantified an iceberg area error at solar zenith angles between 45° and 81° in Greenland, which we finally standardized to the error quantified in the Svalbard experiment.

#### Iceberg area error as a function of resolution

The spatial resolution of remote sensing data and the error of iceberg area retrievals are intrinsically connected. We observed, consistent with other studies (Sulak and others, 2017; Moyer and others, 2019; Rezvanbehbahani and others, 2020), that smaller icebergs exhibit an increased error spread.

The airborne data used to quantify the error magnitude have 6.25 times the resolution of the Sentinel-2 data. Even so, the airborne iceberg areas come with an error. It is reasonable to assume that the increased resolution and the acquisition at the bottom of the atmosphere yield more accurate iceberg areas than the Sentinel-2 retrieval. Figure 12 portrays this difference in resolution by showing the maximum negative and positive  $RE$  examples, and a moderate example. It is unclear why some of the measurements in Fig. 12a fall below the threshold, producing a high negative error. A shadow on the iceberg causes the

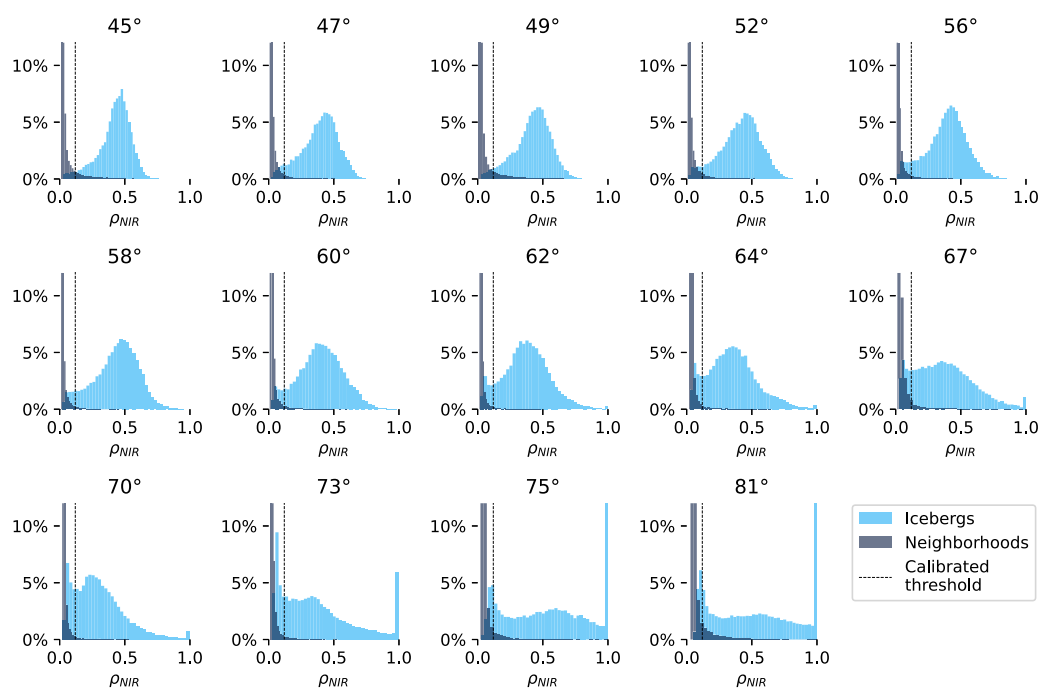


**Figure 9.** Iceberg and neighborhood  $\rho_{NIR}$  histograms at distinct solar zenith angles. The calibrated threshold is shown for reference.



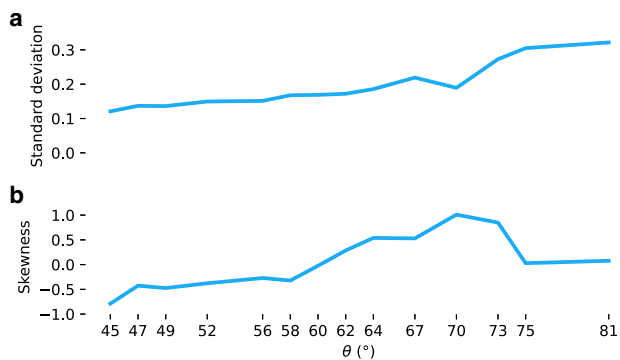


**Figure 10.** The standard deviation (a) and the skewness (b) of the iceberg  $\rho_{NIR}$  measurements by the solar zenith angle.

underestimated iceberg area in Fig. 12b. Adjacent pieces of ice might contribute to the overestimated iceberg area in Fig. 12c. Though, these examples also depict that the iceberg delineation in the Dornier imagery is not undisputed. Another layer of higher resolution data or direct measurements would be needed to quantify this error.

#### Iceberg area error by solar zenith angle

Our standardized iceberg area error  $SRE_{\theta}$  roughly agrees with the 4% overestimation Moyer and others (2019) quantified at a 47° solar zenith angle. The rough agreement seems to confirm the viability of the  $SRE_{\theta}$ .

Nonetheless, it remains debatable how to meaningfully connect the Svalbard  $RE$  to the Greenland  $RE_{\theta}$ . Optimally, we would derive the Svalbard dataset at a range of solar zenith angles, but that was infeasible. The two connected experiments addressed this issue sub-optimally, with drawbacks.

The iceberg areas covered by the two experiments differ fundamentally. The largest iceberg in the Svalbard calibration has half the *root length* of the mean *root length* sampled in Greenland. To discuss this we examined the  $SRE_{\theta}$  spread. As the solar zenith angle increases the slopes on a roughened surface become divided into sun-facing slopes and opposite slopes. The incidence angle of the solar irradiation is lower for the sun-facing slope than for the opposite slope (Gardner and Sharp, 2010). At a different scale

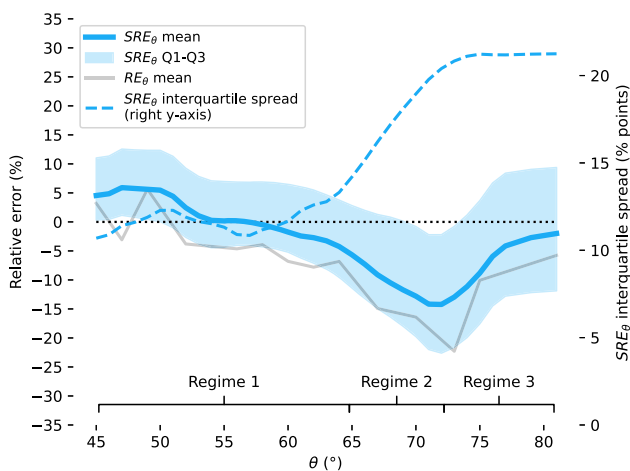


**Figure 11.** The iceberg area errors by the solar zenith angle. The error regimes are denoted above the x-axis. The dashed line corresponds to the light shaded area. The plot contains the  $RE_{\theta}$  (grey line) quantified in Greenland, and the standardized iceberg area error  $SRE_{\theta}$  (blue line) representing the magnitude of the iceberg area error quantified in the Svalbard experiment, and the variation quantified in the Greenland experiment.

than the iceberg roughness, Larue and others (2020) showed that the snow albedo at 1000 nm decreases when increasing the surface roughness. Similarly, Lhermitte and others (2014) observed a decrease in the albedo of glacier ice with increased surface roughness. More so, a slope facing away from the sun might not receive direct solar irradiation, i.e. is shadowed, at a sufficiently high solar zenith angle. This explains the increased spread in the iceberg reflectance and consequently in the  $SRE_{\theta}$  at high solar zenith angles (Figs. 14a, c).

We attribute the spread in the  $SRE_{\theta}$  at a specific solar zenith angle to variations in the meter-scale surface roughness. The first example iceberg at 81° (Fig. 13e) seems to exhibit a rougher surface and some shadowing, whereas the second (Fig. 13f) appears smoother and differently oriented. Particularly at these high solar zenith angles, an increased meter-scale surface roughness is likely to cause a higher negative  $SRE_{\theta}$ . In turn, this variation implies that we succeeded to encompass a variety of surface roughnesses. We propose that this variety at every solar zenith angle is more important than the size diversity with respect to the  $SRE_{\theta}$  variation. Admittedly, we cannot prove this without doubt. Therefore, we emphasize that the  $SRE_{\theta}$  is an approximation in the absence of a better error estimate across solar zenith angles.

#### Implications for optical iceberg area retrievals

We suggest a solar zenith angle of 65° as a sensible, yet not strict, limit for the iceberg area retrieval from Sentinel-2 NIR data. This is 5° below the application-independent recommendation of the European Space Agency (2019), and consistent with Kern (2022) who observed inconsistent illumination on sea ice already below 65°. Above 65° the  $SRE_{\theta}$  implies increasingly underestimated iceberg areas with a widening error spread. These changes correspond to right-skewed iceberg reflectance measurements as the solar zenith angle rises. The observed iceberg reflectance applies independently of the  $SRE_{\theta}$ . Hence high solar zenith angles challenge the iceberg area retrieval from Sentinel-2 near-infrared data and comparable data irrespective of the algorithm used.

It is questionable how adjusting the iceberg reflectance threshold can tackle this problem. Moyer and others (2019) increased the NIR reflectance threshold to 0.3 at a 81° solar zenith angle. Indeed, our study implies underestimated iceberg areas at high solar zenith angles. Hence, a lower threshold would be more sensible to accommodate shadows on the icebergs, in theory. However, without higher resolution reference data, it is difficult to visually distinguish shadows in the Sentinel-2 data from submerged parts of the iceberg, and from the surrounding water. Making this distinction by visual means was only feasible for the large icebergs sampled in the Greenland experiment (Fig. 14).

Ambiguity around suitable iceberg thresholds at high solar zenith angles may arise due to the increased mean iceberg  $\rho_{NIR}$ . However, we showed that the spread in the reflectance widens above 75°. Analyzing the, on average, higher reflectance might suggest raising the threshold, but our experiment implies that this is not a viable solution because it does not accommodate shadows. Moreover, shadows on the icebergs converge with the ocean reflectance, which increases with the solar zenith angle (Pegau and Paulson, 2001). This suggests an increased overlap between the distributions, making it difficult to accommodate shadows on the icebergs.

Still, our study leaves open if a dynamically adjusted threshold could reduce the error margins at low solar zenith angles. Moyer and others (2019) suggested a slightly higher threshold at 47°. We explored this briefly, confirming a threshold above (below) 0.12 below (above) 56°. However, we doubt that our Greenland dataset facilitates deriving such adjusted thresholds reliably. Instead, we



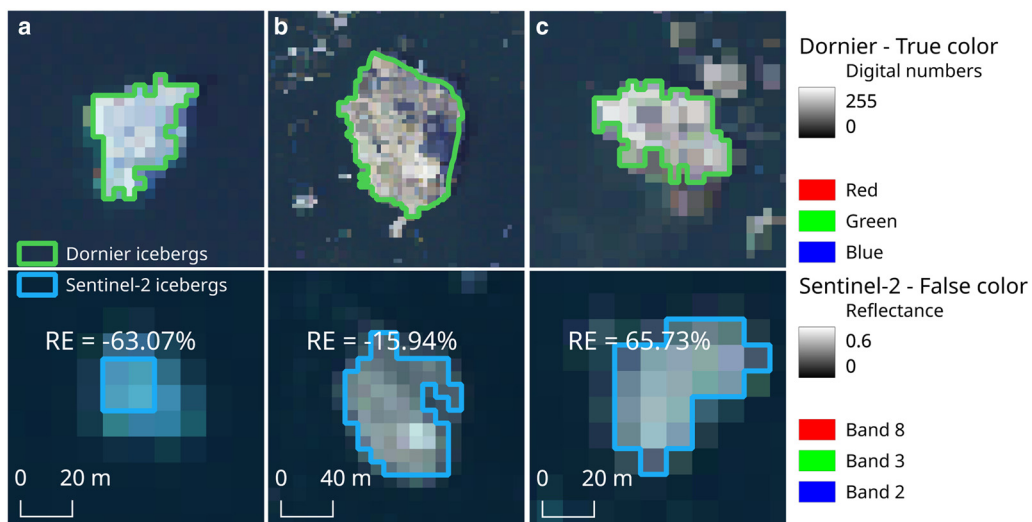


**Figure 12.** Maximum negative iceberg area error (a), a moderate error (b), and the maximum positive iceberg area error (c) obtained in the Svalbard calibration. The icebergs were observed at about 78.589 448 73°N, 19.856 185 13°E with a 722 m drift (a), 78.539 973 04°N, 19.529 583 75°E with a 75 m drift (b), and 78.540 720 6°N, 19.512 837 0°E with a 164 m drift (c). Note that example (a) was located closer to the end of the flight tracks, resulting in a larger time lag between the Sentinel-2 and the Dornier data acquisition.

suggest using the  $SRE_{\theta}$  for potentially correcting iceberg area retrievals. This correction is most viable up to 65° due to the consistency in the error.

### Limits in scope

#### Detection performance

Our study leaves unclear what the detection performance trade-off is between true positive, false positive, and false negative iceberg detections. Reflectance thresholds primarily confuse icebergs with sea ice floes (Sulak and others, 2017; Moyer and others, 2019; Scheick and others, 2019). Thus, the detection performance will largely depend on the setting of the evaluation. Our threshold is not necessarily the best to balance the performance trade-off. A higher threshold likely produces fewer false positive detections (Scheick and others, 2019), in particular with respect to sea ice

floes (Moyer and others, 2019). Though, it may also miss more icebergs. We have examined the impact of high solar zenith angles on the iceberg retrieval, but we have not quantified how the solar zenith angle impacts the detection of icebergs. We expect a suitably-trained convolutional neural network to be more skilled in detecting icebergs particularly in complex ice mélange, as Rezvanbehbahani and others (2020) showed for Planet data. Potentially, a similar machine learning algorithm could be trained on Sentinel-2 data. Training data may be generated by applying the NIR reflectance threshold with a subsequent manual filtering of false detections. We recommend covering a variety of solar zenith angles in the training, but limited to a suitable range.

#### Air temperature

Inherently our study cannot reveal how the area error behaves outside the covered air temperatures. Nearly all data were

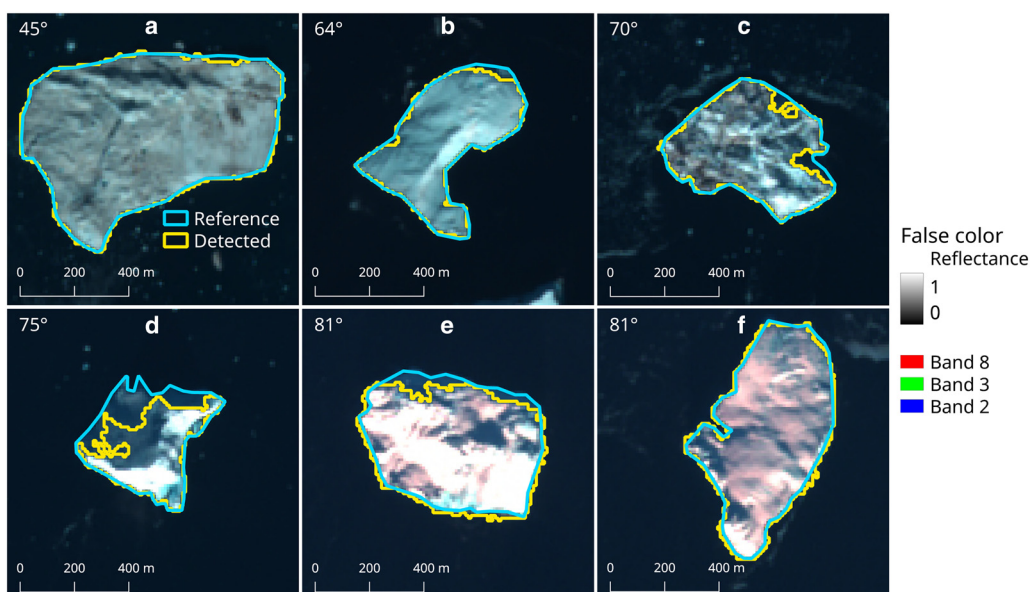


**Figure 13.** Iceberg examples in the Kangerlussuaq Fjord overlaid by the reference outlines and the detected outlines. The icebergs were observed in the Sentinel-2 tile 25WER acquired at 67.947 121 30°N, -31.605 731 89°W. The rising abundance of shadows as  $\theta$  increases results in underestimated iceberg areas (c, d, e). Depending on the surface topography and orientation, the iceberg area may still be accurate at high solar zenith angles (f), which increases the overall spread in the iceberg area error.

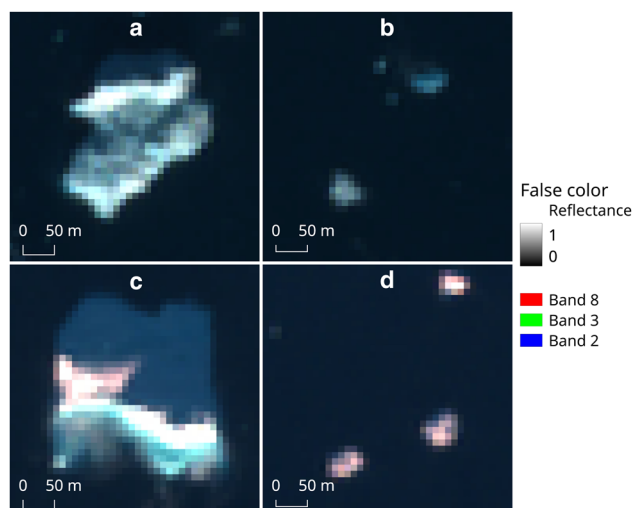


**Figure 14.** Icebergs at  $\theta=67^\circ$  (a, b) on 20 September 2018, and at  $\theta=81^\circ$  on 26 October 2020 (c, d) in the Kangerlussuaq Fjord. The iceberg locations are  $68.002\ 306^\circ\text{N}$ ,  $-31.911\ 890^\circ\text{W}$  (a),  $68.002\ 306^\circ\text{N}$ ,  $-31.911\ 890^\circ\text{W}$  (b),  $67.990\ 706\ 0^\circ\text{N}$ ,  $-31.874\ 126\ 7^\circ\text{W}$  (c), and  $68.409\ 449\ 9^\circ\text{N}$ ,  $-32.333\ 919\ 4^\circ\text{W}$  (d). The maps show the segregation into shadows and bright sun-facing slopes. The effect is recognizable on small icebergs (b, d), but the resolution impedes a reliable delineation.

obtained at positive air temperatures. The drop in the iceberg reflectance on 28 September 2021 coincides with the maximum mean air temperature obtained in the dataset. Still, despite an air temperature slightly above freezing, the  $RE_\theta$  is similar on the 6 October 2021. This is a weak sign that the air temperature might be negligible concerning iceberg areas, at least at the mostly positive temperatures in our study. Indeed, we cannot prove this, and we had limited samples below freezing.

### Outlook

The results of the presented study may help limit iceberg studies to suitable solar zenith angles, and correct iceberg area retrievals. This knowledge is valuable for applying the method on a larger spatial and temporal scale. However, other errors are important to take into account when calculating total iceberg areas. In particular, sea ice floes are likely to be wrongly identified as icebergs. Sulak and others (2017) proposed statistically correcting for sea ice, although this requires additional knowledge of the local sea ice proportion. Automatically distinguishing icebergs from sea ice would not only be beneficial for automating the iceberg detection, but also to quantify the composition of ice mélange.

The iceberg calving term accounts for a large amount of the uncertainties in the glacial mass balance in marine-terminating glaciers (Alley and others, 2023). Improving and further validating the iceberg area retrieval from satellite data is therefore important, although information on iceberg areas alone is insufficient to quantify the calving volume. We hence emphasize connecting observations of iceberg populations and ice mélange to observed and modeled changes in the glacier termini (Foga and others, 2014; Amaral and others, 2020; Wehrlé and others, 2023) on extended spatial and temporal scales. We suggest utilizing both synthetic aperture radar data and optical data for retrieving iceberg areas.

### Conclusions

We approximated the error in iceberg area retrievals from top-of-atmosphere Sentinel-2 near-infrared reflectance data at solar zenith angles between  $45^\circ$  and  $81^\circ$ . Our study proposes a

Sentinel-2 near-infrared reflectance threshold for detecting and delineating icebergs, and it provides the error in the area retrieval with varying solar zenith angles. We recommend applying the proposed threshold up to a solar zenith angle of  $65^\circ$ . Meanwhile, we emphasize general limitations of a constant reflectance threshold, in particular its inability to reliably distinguish icebergs from sea ice. To conclude:

1. The iceberg area retrieval is consistent up to a solar zenith angle of  $65^\circ$ .
2. At a solar zenith angle of  $56^\circ$ , the NIR reflectance threshold of 0.12 yields the most accurate iceberg areas.
3. Iceberg areas sizes are increasingly underestimated with a rising solar zenith angle, and the error spread increases.
4. Shadows formed by the meter-scale iceberg surface roughness and its orientation are the main error sources at high solar zenith angles.

**Data.** The code written to conduct this study is available on GitHub: <https://github.com/hfisser/S2-iceberg-areas>. Data can be requested from the corresponding author.

**Acknowledgements.** The authors wish to acknowledge the support from the Research Council of Norway through the RareIce project (326834) and the support from all RareIce partners.

We are thankful for the valuable data provided by the Copernicus program of the European Commission, and by the Svalbard Integrated Arctic Earth Observing System (SIOS). This study contains modified Copernicus Sentinel data (2016–2021) and modified Copernicus Climate Change Service information (2016–2021). This study contains airborne data retrieved through SIOS (2020).

**Author contributions.** HF performed all calculations and wrote most of the paper, HF processed and analyzed the data, HF, APD, and KVH designed the research, and contributed to writing and editing the paper.

### References

- Alley R and 8 others (2023) Iceberg calving: regimes and transitions. *Annual Review of Earth and Planetary Sciences* 51(1), 189–215. doi: [10.1146/annurev-earth-032320-110916](https://doi.org/10.1146/annurev-earth-032320-110916)
- Amaral T, Bartholomaeus TC and Enderlin EM (2020) Evaluation of iceberg calving models against observations from Greenland outlet glaciers. *Journal of Geophysical Research: Earth Surface* 125(6), e2019JF005444. doi: [10.1029/2019JF005444](https://doi.org/10.1029/2019JF005444)
- Azetsu-Scott K and Syvitski JPM (1999) Influence of melting icebergs on distribution, characteristics and transport of marine particles in an East Greenland fjord. *Journal of Geophysical Research: Oceans* 104(C3), 5321–5328. doi: [10.1029/1998JC900083](https://doi.org/10.1029/1998JC900083)
- Bhatia MP and 5 others (2013) Greenland meltwater as a significant and potentially bioavailable source of iron to the Ocean. *Nature Geoscience* 6(4), 274–278. doi: [10.1038/ngeo1746](https://doi.org/10.1038/ngeo1746)
- Bigg GR, Wadley MR, Stevens DP and Johnson JA (1997) Modelling the dynamics and thermodynamics of icebergs. *Cold Regions Science and Technology* 26(2), 113–135. doi: [10.1016/S0165-232X\(97\)00012-8](https://doi.org/10.1016/S0165-232X(97)00012-8)
- Bobby P and Power D (2023) Advances in satellite technology for ice management. In *Day 3 Wed, May 03, 2023*, D031S111R003. Houston, Texas, USA: OTC.
- Buus-Hinkler J, Qvistgaard K and Krane KAH (2014) Iceberg number density—Reaching a full picture of the Greenland waters. In *2014 IEEE Geoscience and Remote Sensing Symposium*. Quebec City, QC: IEEE, pp. 270–273.
- Copernicus Climate Change Service (C3S) Climate Data Store (2021) Arctic regional reanalysis on single levels from 1991 to present.
- Dierking W and Wesche C (2014) C-band radar polarimetry—useful for detection of icebergs in sea ice?. *IEEE Transactions on Geoscience and Remote Sensing* 52(1), 25–37. doi: [10.1109/TGRS.2012.2234756](https://doi.org/10.1109/TGRS.2012.2234756)
- Duprat LPAM, Bigg GR and Wilton DJ (2016) Enhanced southern Ocean marine productivity due to fertilization by giant icebergs. *Nature Geoscience* 9(3), 219–221. doi: [10.1038/ngeo2633](https://doi.org/10.1038/ngeo2633)

- Enderlin EM and 5 others (2014) An improved mass budget for the Greenland ice sheet. *Geophysical Research Letters* **41**(3), 866–872. doi: [10.1002/2013GL059010](https://doi.org/10.1002/2013GL059010)
- ESA (2023) Sentinel-2 MSI user guide. Available at <https://sentinels.copernicus.eu/web/sentinel/user-guides/sentinel-2-msi>.
- ESA (2024) S2 processing. Available at <https://sentiwiki.copernicus.eu/web/s2-processing>.
- European Space Agency (2019) Copernicus Sentinel-2 observation in low illumination conditions over Northern Europe and Arctic Areas.
- Foga S, Stearns LA, Van Der Veen C (2014) Application of satellite remote sensing techniques to quantify terminus and ice Mélange behavior at Helheim Glacier, East Greenland. *Marine Technology Society Journal* **48**(5), 81–91. doi: [10.4031/MTSJ.48.5.3](https://doi.org/10.4031/MTSJ.48.5.3)
- Færch L, Dierking W, Hughes N and Doulgeris AP (2023) A comparison of constant false alarm rate object detection algorithms for iceberg identification in L- and C-band SAR imagery of the Labrador sea. *The Cryosphere* **17**(12), 5335–5355. doi: [10.5194/tc-17-5335-2023](https://doi.org/10.5194/tc-17-5335-2023)
- Gardner AS and Sharp MJ (2010) A review of snow and ice albedo and the development of a new physically based broadband albedo parameterization. *Journal of Geophysical Research* **115**(F1), F01009. doi: [10.1029/2009JF001444](https://doi.org/10.1029/2009JF001444)
- Huang CJ, Qiao F, Chen S, Xue Y and Guo J (2019) Observation and parameterization of broadband sea surface albedo. *Journal of Geophysical Research: Oceans* **124**(7), 4480–4491. doi: [10.1029/2018JC014444](https://doi.org/10.1029/2018JC014444)
- Keghouche I, Counillon F and Bertino L (2010) Modeling dynamics and thermodynamics of icebergs in the Barents sea from 1987 to 2005. *Journal of Geophysical Research: Oceans* **115**(C12), 2010JC006165. doi: [10.1029/2010JC006165](https://doi.org/10.1029/2010JC006165)
- Kern S (2022) Satellite passive microwave sea-ice concentration data set inter-comparison using Landsat data. *The Cryosphere* **16**(1), 349–378. doi: [10.5194/tc-16-349-2022](https://doi.org/10.5194/tc-16-349-2022)
- Kirkham JD (2017) Drift-dependent changes in iceberg size-frequency distributions. *Scientific Reports* **7**(1), 15991. doi: [10.1038/s41598-017-14863-2](https://doi.org/10.1038/s41598-017-14863-2)
- Koltzow M, Schyberg H, Støylen E and Yang X (2022) Value of the copernicus arctic regional reanalysis (CARRA) in representing near-surface temperature and wind speed in the north-east European Arctic. *Polar Research* **41**. doi: [10.33265/polar.v41.8002](https://doi.org/10.33265/polar.v41.8002)
- König M, Hieronymi M and Oppelt N (2019) Application of Sentinel-2 MSI in arctic research: evaluating the performance of atmospheric correction approaches over Arctic Sea Ice. *Frontiers in Earth Science* **7**, 22. doi: [10.3389/feart.2019.00022](https://doi.org/10.3389/feart.2019.00022)
- Larue F and 8 others (2020) Snow albedo sensitivity to macroscopic surface roughness using a new ray-tracing model. *The Cryosphere* **14**(5), 1651–1672. doi: [10.5194/tc-14-1651-2020](https://doi.org/10.5194/tc-14-1651-2020)
- Lhermitte S, Abermann J and Kinnard C (2014) Albedo over rough snow and ice surfaces. *The Cryosphere* **8**(3), 1069–1086. doi: [10.5194/tc-8-1069-2014](https://doi.org/10.5194/tc-8-1069-2014)
- Marchenko A, Diansky N and Fomin V (2019) Modeling of iceberg drift in the marginal ice zone of the Barents Sea. *Applied Ocean Research* **88**, 210–222. doi: [10.1016/j.apor.2019.03.008](https://doi.org/10.1016/j.apor.2019.03.008)
- Marino A, Dierking W and Wesche C (2016) A depolarization ratio anomaly detector to identify icebergs in sea ice using dual-polarization SAR images. *IEEE Transactions on Geoscience and Remote Sensing* **54**(9), 5602–5615. doi: [10.1109/TGRS.2016.2569450](https://doi.org/10.1109/TGRS.2016.2569450)
- Monteban D, Lubbad R, Samardzija I and Løset S (2020) Enhanced iceberg drift modelling in the Barents Sea with estimates of the release rates and size characteristics at the major glacial sources using Sentinel-1 and Sentinel-2. *Cold Regions Science and Technology* **175**, 103084. doi: [10.1016/j.coldregions.2020.103084](https://doi.org/10.1016/j.coldregions.2020.103084)
- Moon T and 5 others (2018) Subsurface iceberg melt key to Greenland fjord freshwater budget. *Nature Geoscience* **11**(1), 49–54. doi: [10.1038/s41561-017-0018-z](https://doi.org/10.1038/s41561-017-0018-z)
- Moyer AN, Sutherland DA, Nienow PW and Sole AJ (2019) Seasonal variations in iceberg freshwater flux in sermilik fjord, Southeast Greenland from Sentinel-2 imagery. *Geophysical Research Letters* **46**(15), 8903–8912. doi: [10.1029/2019GL082309](https://doi.org/10.1029/2019GL082309)
- Neuhaus SU, Tulaczyk SM and Branecky Begeman C (2019) Spatiotemporal distributions of icebergs in a temperate fjord: Columbia Fjord, Alaska. *The Cryosphere* **13**(7), 1785–1799. doi: [10.5194/tc-13-1785-2019](https://doi.org/10.5194/tc-13-1785-2019)
- Pegau WS and Paulson CA (2001) The albedo of Arctic leads in summer. *Annals of Glaciology* **33**, 221–224. doi: [10.3189/172756401781818833](https://doi.org/10.3189/172756401781818833)
- Power D, Youden J, Lane K, Randell C and Flett D (2001) Iceberg detection capabilities of RADARSAT synthetic aperture radar. *Canadian Journal of Remote Sensing* **27**(5), 476–486. doi: [10.1080/07038992.2001.10854888](https://doi.org/10.1080/07038992.2001.10854888)
- Rezvanbehbahani S, Stearns LA, Keramati R, Shankar S, Van Der Veen CJ (2020) Significant contribution of small icebergs to the freshwater budget in Greenland fjords. *Communications Earth & Environment* **1**(1), 31. doi: [10.1038/s43247-020-00032-3](https://doi.org/10.1038/s43247-020-00032-3)
- Robock A (1980) The seasonal cycle of snow cover, sea ice and surface albedo. *Monthly Weather Review* **108**(3), 267–285. doi: [10.1175/1520-0493\(1980\)108<0267:TSCOSC>2.0.CO;2](https://doi.org/10.1175/1520-0493(1980)108<0267:TSCOSC>2.0.CO;2)
- Scheick J, Enderlin EM and Hamilton G (2019) Semi-automated open water iceberg detection from Landsat applied to Disko Bay, West Greenland. *Journal of Glaciology* **65**(251), 468–480. doi: [10.1017/jog.2019.23](https://doi.org/10.1017/jog.2019.23)
- Schild KM, Sutherland DA, Elosegui P and Duncan D (2021) Measurements of iceberg melt rates using high-resolution GPS and iceberg surface scans. *Geophysical Research Letters* **48**(3), e2020GL089765. doi: [10.1029/2020GL089765](https://doi.org/10.1029/2020GL089765)
- Schyberg H (2020) Arctic regional reanalysis on single levels from 1991 to present. Copernicus Climate Change Service (C3S) Climate Data Store (CDS).
- Shiggins CJ, Lea JM and Brough S (2023) Automated ArcticDEM iceberg detection tool: insights into area and volume distributions, and their potential application to satellite imagery and modelling of glacier–ocean systems. *The Cryosphere* **17**(1), 15–32. doi: [10.5194/tc-17-15-2023](https://doi.org/10.5194/tc-17-15-2023)
- Skakun S (2022) Cloud mask intercomparison eXercise (CMIX): an evaluation of cloud masking algorithms for Landsat 8 and Sentinel-2. *Remote Sensing of Environment* **274**, 112990. doi: [10.1016/j.rse.2022.112990](https://doi.org/10.1016/j.rse.2022.112990)
- Soldad I, Dierking W, Korosov A and Marino A (2019) Automatic detection of small icebergs in fast ice using satellite wide-swath SAR images. *Remote Sensing* **11**(7), 806. doi: [10.3390/rs11070806](https://doi.org/10.3390/rs11070806)
- Stafford B (2023) Pysolar Python package.
- Sulak DJ, Sutherland DA, Enderlin EM, Stearns LA and Hamilton GS (2017) Iceberg properties and distributions in three Greenlandic fjords using satellite imagery. *Annals of Glaciology* **58**(74), 92–106. doi: [10.1017/aog.2017.5](https://doi.org/10.1017/aog.2017.5)
- Sutherland DA and 8 others (2019) Direct observations of submarine melt and subsurface geometry at a tidewater glacier. *Science* **365**(6451), 369–374. doi: [10.1126/science.aax3528](https://doi.org/10.1126/science.aax3528)
- Tao D, Doulgeris AP and Brekke C (2016) A segmentation-based CFAR detection algorithm using truncated statistics. *IEEE Transactions on Geoscience and Remote Sensing* **54**(5), 2887–2898. doi: [10.1109/TGRS.2015.2506822](https://doi.org/10.1109/TGRS.2015.2506822)
- Warren SG (2019) Optical properties of ice and snow. *Philosophical Transactions of the Royal Society A: Mathematical, Physical and Engineering Sciences* **377**(2146), 20180161. doi: [10.1098/rsta.2018.0161](https://doi.org/10.1098/rsta.2018.0161)
- Wehrlé A, Lüthi MP and Vieli A (2023) The control of short-term ice mélange weakening episodes on calving activity at major Greenland outlet glaciers. *The Cryosphere* **17**(1), 309–326. doi: [10.5194/tc-17-309-2023](https://doi.org/10.5194/tc-17-309-2023)
- Whicker CA and 5 others (2022) SNICAR-ADV4: a physically based radiative transfer model to represent the spectral albedo of glacier ice. *The Cryosphere* **16**(4), 1197–1220. doi: [10.5194/tc-16-1197-2022](https://doi.org/10.5194/tc-16-1197-2022)
- Williams R and Macdonald M (1995) An image segmentation technique to infer the outlines of icebergs, depicted in satellite images, from their shadows and bright sunlit surfaces. In *Proceedings of Third Australian and New Zealand Conference on Intelligent Information Systems*. ANZIIS-95. Perth, WA, Australia: IEEE, pp. 76–81.